



|                                  |   |
|----------------------------------|---|
| <b>Publication Year</b>          | 2019  |
| <b>Acceptance in OA</b>          | 2021-02-25T10:56:10Z  |
| <b>Title</b>                     | Surface Temperatures and Water Ice Sublimation Rate of Oxo Crater: A Comparison With Juling Crater                |
| <b>Authors</b>                   | FORMISANO, Michelangelo, Federico, C., Magni, G., RAPONI, Andrea, DE SANCTIS, MARIA CRISTINA, FRIGERI, ALESSANDRO |
| <b>Publisher's version (DOI)</b> | 10.1029/2018JE005839  |
| <b>Handle</b>                    | <a href="http://hdl.handle.net/20.500.12386/30610">http://hdl.handle.net/20.500.12386/30610</a>                   |
| <b>Journal</b>                   | JOURNAL OF GEOPHYSICAL RESEARCH (PLANETS)   |
| <b>Volume</b>                    | 124   |

## RESEARCH ARTICLE

10.1029/2018JE005839

## Surface Temperatures and Water Ice Sublimation Rate of Oxo Crater: A Comparison With Juling Crater

## Special Section:

Ice on Ceres

 M. Formisano<sup>1</sup> , C. Federico<sup>1</sup>, G. Magni<sup>1</sup>, A. Raponi<sup>1</sup> , M.C. De Sanctis<sup>1</sup> , and A. Frigeri<sup>1</sup> 
<sup>1</sup>INAF-IAPS, Rome, Italy

## Key Points:

- We calculated the surface temperature and sublimation rates of Oxo crater by applying a 3-D thermophysical model on real topography
- We compared the simulated temperatures with the VIR measurements
- Water emission rate suggests that Oxo is not the source of the emission detected by Herschel, while Juling probably is the best candidate

## Supporting Information:

- Supporting Information S1

## Correspondence to:

 M. Formisano,  
michelangelo.formisano@iaps.inaf.it

## Citation:

 Formisano, M., Federico, C., Magni, G., Raponi, A., De Sanctis, M.-C., & Frigeri, A. (2019). Surface temperatures and water ice sublimation rate of Oxo crater: A comparison with Juling crater. *Journal of Geophysical Research: Planets*, 124, 2–13. <https://doi.org/10.1029/2018JE005839>

Received 4 OCT 2018

Accepted 6 DEC 2018

Accepted article online 10 DEC 2018

Published online 3 JAN 2019

**Abstract** Dwarf planet Ceres is characterized by several sites hosting (or have hosted) ice-rich patches as revealed by the Dawn's Visible and InfraRed spectrometer. The study of the illumination conditions including the effects of the local topography become critical in the estimation of the ice lifetime as well as the water vapor production rate. In this work we applied a 3-D thermophysical model in order to study the illumination conditions on the shape model, derived on the basis of the images acquired by the Dawn's Framing Camera during the Survey mission phase, and to calculate the surface temperatures and water sublimation rates. We are interested in a crater in the northern hemisphere (42°), Oxo, which hosts water ice in its southern wall. A comparison with the surface temperatures and water sublimation rates of another Ceres' crater, Juling, is carried out. Water ice sublimation rate of its ice-rich patch suggests that the Oxo crater probably is not the source of the emission detected by Herschel, a source that could be represented instead by the Juling crater.

**Plain Language Summary** There are several reasons to support the idea that the dwarf planet Ceres is a world with a huge presence of water. First of all, spectral evidence of water ice has been revealed by the Dawn's Visible and InfraRed spectrometer on the wall of some craters. Furthermore, both geomorphological evidence like surface flows and the presence of minerals, whose origin is correlated to the aqueous alteration, support this idea. Numerical simulations could contribute to understand how long the ice is stable on the surface, by studying the illumination conditions, and quantifies the eventual sublimation rate. In this work we concern about a particular crater, Oxo, in the northern hemisphere at latitude 42°, which hosts an ice-rich patch in the southern wall.

## 1. Introduction

Several locations on the surface of the dwarf planet Ceres are characterized by the presence of water ice. Recently, Combe et al. (2018) have identified nine locations that exhibit bands of the H<sub>2</sub>O molecule at 2.00, 1.65, and 1.28 μm and all these locations are at latitude poleward >30°. Among these locations are Juling (Raponi, De Sanctis, Frigeri, et al., 2018), Oxo (Combe et al., 2016), and a small crater, Zatik, whose latitude is 70° N (Ermakov et al., 2017; Platz et al., 2016).

The presence of water ice on the surface/subsurface of Ceres is also supported by geomorphological evidence (surface flow; Schmidt et al., 2017), by the Dawn's Gamma-Ray and Neutron Detector measurements of hydrogen (Prettyman et al., 2017), and by the inferred upper crust stratigraphy (Nathues et al., 2016). A content of 30–40% of weak phase (water and/or porosity) in the shallow subsurface has also been inferred by Bland et al. (2016), while Fu et al. (2017) fixed the volume content of water ice in the crust at <25%. The estimated mean value of the bulk density, that is, 2,162 kg m<sup>-3</sup> (Park et al., 2016; Russell et al., 2016), is another data that supports the idea of a large fraction of water ice in Ceres' interior. Recent thermophysical models (Ermakov et al., 2017; Fu et al., 2017; Konopliv et al., 2018) have suggested that the crust (≈45 km) has a density ranging from 1,200 to 1,600 kg m<sup>-3</sup> compatible with no more than ≈30 vol.% of ice. King et al. (2018) estimated a crustal density <1,300 kg m<sup>-3</sup> consistent with hydrothermal alteration and also suggested the presence of a dense core (2,367 kg m<sup>-3</sup> and 100 km in size). Thermophysical models, developed in the past (Castillo-Rogez & McCord, 2010; McCord & Sotin, 2005), conversely, estimated a quantity of free water by mass from 17% to 27%. In addition, the existence of some specific minerals produced by aqueous alteration seems to confirm the presence of water ice in the subsurface layers (Carrozzo et al., 2018; Ciarniello et al., 2017; De Sanctis et al., 2016; McSween et al., 2018).

Küppers et al. (2014) reported the Herschel observations of water vapor (6 kg/s) around Ceres, probably emitted by a localized midlatitude region, while A'Hearn and Feldman (1992) provided measurements about the detection of  $\text{OH}^-$ , a product of photodissociation of water. Therefore, it is important to understand how the ice-rich patches on Ceres' surface are activated. Several proposals can be found in the literature: cometary-type sublimation (Fanale & Salvail, 1987; Formisano, De Sanctis, et al., 2016), impacts with other bodies (A'Hearn & Feldman, 1992), cryovolcanism (Neveu & Desch, 2015), energetic solar flares (Villarreal et al., 2017), and crust gravitational overturn (Formisano, Federico, et al., 2016). The water vapor released can contribute to form a transient exosphere around Ceres, whose timescale is less than 1 week (Formisano, De Sanctis, et al., 2016), while Schorghofer et al. (2017) give, under different thermophysical assumptions, a shorter estimation ( $\approx 7$  hr). How long the ice survives on Ceres' surface and what is the expected water vapor production are questions that some previous thermophysical models have already tried to address. For example, Hayne and Aharonson (2015) estimated that water ice is stable for 1,000 years at latitudes  $<30^\circ$  in case of low thermal inertia. Formisano, De Sanctis, et al. (2016) suggested that exposed ice is stable for few orbits and an agreement with Herschel observations is reached if ice is buried a few centimeters below the surface with an emitting area of  $\approx 100 \text{ km}^2$ . Also, Landis et al. (2017) studied the thermophysical conditions to have an emission compatible with Herschel measurements, determining that buried ice alone cannot explain the measured water vapor rate, and it is also necessary to have exposed ice in "favorable" thermophysical conditions. Titus (2015) found that water ice is unstable at low latitudes but could be stable at latitudes higher than  $40\text{--}60^\circ$  under a "right" combination of physical parameters. Finally, Schorghofer et al. (2016) estimated that in the northern hemisphere a region of  $\approx 1,800 \text{ km}^2$  is permanently in shadow. This region could host other ice-rich areas (Platz et al., 2016).

Water presence on Ceres' surface makes this dwarf planet a link between the outer solar system icy satellites and the inner solar system rocky asteroids. The possibility of a seasonal cycle of the water in Ceres has been investigated by Raponi, De Sanctis, Carrozzo, et al. (2018), in which an increase of the water abundance on the northern wall of the crater Juling is reported. This evidence would be the "increasing part" of a more general water ice cycle, which would make Ceres an active icy world. Water ice could sublimate according a quasi cometary-type emission (emission rate increases approaching the Sun), even if the Ceres' gravity is greater than the gravity of a typical comet, and as a consequence, dust particles would be hardly removed from the surface. To constraint the lifetime of surface water ice as well as the surface temperatures and sublimation rate it is crucial to take into account the topography of the location under study. For this purpose, in this work, we used a shape model derived on the basis of the images acquired by the Dawn's Framing Camera during the survey mission phase (Preusker et al., 2016) and we focused on the Oxo crater localized in the northern hemisphere ( $42^\circ$ ). It is a  $\approx 10\text{-km}$ -diameter impact crater located in the rim of a degraded  $\approx 40\text{-km}$ -diameter crater. Oxo is very young, certified by the presence of only few superimposed craters (Nathues et al., 2017), and it is characterized by the presence of an ice-rich coverage of  $\approx 7 \text{ km}^2$  in its southern wall (Combe et al., 2016, 2018) revealed by the observations of the Dawn's Visible and InfraRed Spectrometer.

We applied a 3-D finite element method thermophysical model, taking into account both the self-heating between the facets and the shadowing effects (by using the hemicube method). Planetary rotation is performed by applying a rotational matrix to the 3-D object constructed starting from the shape model. This approach lead us to study in detail the thermophysics of this particular location on Ceres' surface. We also provided a comparison with the surface temperatures and water sublimation rates of another crater, Juling, which hosts water ice on its northern wall (Raponi, De Sanctis, Carrozzo, et al., 2018).

To proceed in our investigation we have selected two different heliocentric distances, 2.71 and 2.96 AU. The first distance is compatible with the Herschel's observations of water vapor (Küppers et al., 2014), the second is linked to the Dawn's VIR measurements (Raponi, De Sanctis, Carrozzo, et al., 2018). In the first case we also explored the effects of the thermal inertia on the surface temperatures and sublimation rates, adopting two different values of the thermal inertia: 500 TIU (case A1) and 15 TIU (case A2). For the second distance, that is, 2.96 AU, for comparison we have used VIR data and we have explored only the case with thermal inertia equal to 15 TIU. This value has been chosen since it is largely present in literature (Hayne & Aharonson, 2015; Landis et al., 2017; Rivkin et al., 2011; Schorghofer et al., 2017). For a detailed discussion about the thermal inertia estimation see also Titus (2015). In order to determine the effects of an extreme value, we have chosen 500 TIU. The physical characteristics of the different scenarios are reported in Table 1.

**Table 1**  
Scenarios We Developed in This Study

| Scenario | Distance (AU) | Solar constant ( $\text{W m}^{-2}$ ) | Subsolar point latitude ( $^{\circ}$ ) | Thermal inertia (TIU) |
|----------|---------------|--------------------------------------|--|-----------------------|
| A1       | 2.71          | 186                                  | -2.2                                   | 500                   |
| A2       | 2.71          | 186                                  | -2.2                                   | 15                    |
| A3       | 2.96          | 155                                  | +2.1                                   | 15                    |

Note. We report the heliocentric distance in astronomical unit, the solar constant scaled for the distance, the subsolar point, and the thermal inertia.

## 2. Numerical Model

### 2.1. Overview

We adopt a 3-D finite element method code by using the software COMSOL Multiphysics 5.3a (www.comsol.com), in particular, the module “Heat Transfer in Solids” with “surface-to-surface radiation” to solve the heat equation, with no convection since we are interested only in surface/subsurface temperatures:

$$\rho(r)c_p(r, T)\frac{\partial T}{\partial t} = \vec{\nabla} \cdot (K(r, T)\vec{\nabla}T), \quad (1)$$

where  $T$  is the temperature,  $t$  the time,  $\rho(r)$  the density,  $c_p(r, T)$  is the specific heat, and  $K(r, T)$  is the thermal conductivity.

The boundary condition we solve for each facet, following, for example, Keller et al. (2015) and Shi et al. (2016), is

$$S_c(1 - a)\cos(Z) + Q_{SH} = -\vec{n} \cdot (K(r, T)\vec{\nabla}T) + fL(T)\Gamma(T) + \varepsilon\sigma T^4, \quad (2)$$

where  $S_c$  is the solar constant scaled for the Ceres’ heliocentric distance in watts per square meter,  $a$  is the albedo,  $\cos(Z)$  is the cosine of the solar incidence,  $\varepsilon$  is the emissivity,  $f$  is the area fraction covered by ice,  $\sigma$  the Stefan-Boltzmann constant,  $L(T)$  is the latent heat of sublimation, and finally,  $\Gamma(T)$  is the sublimation rate. We treat Ceres’ surface as a diffuse surface, which absorbs the solar irradiation and emitted infrared radiation as a gray body with an emissivity of 0.97, an approach similar to Komle et al. (2017). The term  $Q_{SH}$  is the term related to the so-called *self-heating*, that takes into account the mutual radiative interaction (infrared emission and reflected light) among the facets of the integration domain.

Sublimation rate ( $\text{kg}\cdot\text{m}^{-2}\cdot\text{s}^{-1}$ ) is provided by using the following formula (Delsemme & Miller, 1971):

$$\Gamma = p_{\text{sat}}(T)\sqrt{\frac{\mu}{2\pi RT}}, \quad (3)$$

where  $\mu$  is water molar mass,  $R$  the universal gas constant, and  $p_{\text{sat}}(T)$  the water ice saturation pressure, given by (Murphy & Koop, 2005)

$$p_{\text{sat}}(T) = \exp\left[9.550426 - \frac{5723.265}{T} + 3.3068\ln(T) - 0.00728332\right], \quad (4)$$

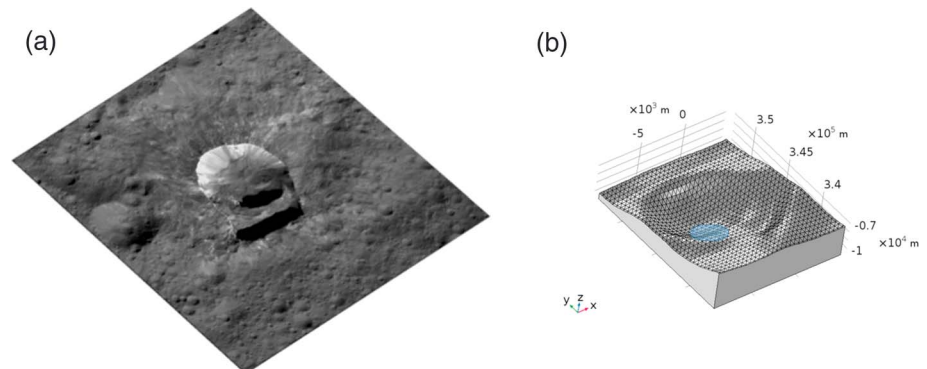


**Figure 1.** (a) Ceres’ surface containing the Oxo crater. (b) Three-dimensional reconstruction of the Oxo crater with the software COMSOL Multiphysics. Cartesian axes are displayed.

**Table 2**  
Physical Parameters Used in This Study

| Parameters                       | Symbol               | Value  | Reference   |
|----------------------------------|----------------------|--|---|
| <b>General</b>                   |                      |  |   |
| Solar constant at Earth distance | $S$                  | 1,361 W m <sup>-2</sup>                            | —   |
| Rotational period                | $\tau$               | 9.074 hr   | Russell et al. (2016)                                     |
| Initial temperature              | $T_0$                | 160 K  | Formisano et al. (2018)                                   |
| Rock volumetric concentration    | $vf_{\text{rock}}$   | 0.85   | Raponi, De Sanctis, et al. (2017)                         |
| Ice volumetric concentration     | $vf_{\text{ice}}$    | 0.15   | Raponi, De Sanctis, et al. (2017)                         |
| <b>Rock</b>                      |                      |  |   |
| Albedo                           | $a_{\text{rock}}$    | 0.03   | Ciarniello et al. (2017); Li et al. (2016)                |
| Density                          | $\rho_{\text{rock}}$ | 1,600 kg m <sup>-3</sup>                           | Heiken et al. (1991)                                      |
| Specific heat                    | $c_{p,\text{rock}}$  | 760 J·kg <sup>-1</sup> ·K <sup>-1</sup>            | Heiken et al. (1991)                                      |
| Thermal conductivity             | $K_{\text{rock}}$    | 2 W·m <sup>-1</sup> ·K <sup>-1</sup>               | Heiken et al. (1991)                                      |
| <b>Ice</b>                       |                      |  |   |
| Albedo <sup>a</sup>              | $a_{\text{ice}}$     | 0.09   | Raponi, Carrozzo, et al. (2017); Ciarniello et al. (2017) |
| Density                          | $\rho_{\text{ice}}$  | 950 kg m <sup>-3</sup>                             | —   |
| Specific heat                    | $c_{p,\text{ice}}$   | 7.037T + 185.0 J·kg <sup>-1</sup> ·K <sup>-1</sup> | Ellsworth and Schubert (1983)                             |
| Thermal conductivity             | $K_{\text{ice}}$     | 567/T W·m <sup>-1</sup> ·K <sup>-1</sup>           | Klinger (1980)  |
| Enthalpy of sublimation          | $L(T)$               | 51.058 kJ kg <sup>-1</sup>                         | Murphy and Koop (2005)                                    |

*Note.* The ice-rich patch is modeled as a mixture of 85% of rock and 15% of ice. Density, specific heat, and thermal conductivity of the patch are calculated according to these percentages.

<sup>a</sup>This value refers to the mixture ice-rock adopted in the ice-rich patch.

valid for  $T > 110$  K. We set the initial temperature of Oxo at 160 K, which is approximately the radiation equilibrium temperature of Ceres at its average heliocentric distance. The ice-rich region (Combe et al., 2018; Raponi et al., 2016) shown in blue in Figure 1 is modeled assuming 85% of “rock” and 15% of water ice (see Table 2 for the physical properties of the materials). In the remaining part of the surface, the percentage of water ice is considered negligible. The estimated area covered by water ice by VIR is  $\simeq 7$  km<sup>2</sup> (Combe et al., 2018). The physical quantities of the ice-rock mixture in the ice-rich patch are weighted by volume (density and thermal conductivity) and by mass (specific heat), as follows:

$$\rho_{\text{mix}} = vf_{\text{ice}}\rho_{\text{ice}} + vf_{\text{rock}}\rho_{\text{rock}}, \quad (5)$$

$$K_{\text{mix}} = vf_{\text{ice}}K_{\text{ice}} + vf_{\text{rock}}K_{\text{rock}}, \quad (6)$$

$$c_{p,\text{mix}} = mf_{\text{ice}}c_{p,\text{ice}} + mf_{\text{rock}}c_{p,\text{rock}}, \quad (7)$$

where  $vf_{\text{ice}}$  and  $vf_{\text{rock}}$  are the volumetric percentages of ice and rock, while  $mf_{\text{ice}}$  and  $mf_{\text{rock}}$  are the mass percentages. As in Formisano et al. (2018), we corrected the thermal conductivity with the Hertz factor, which is defined as the ratio between the grain-to-grain area of contact and the cross section of the grains. The variability of the Hertz factor ranges from 0.1 to  $10^{-4}$ , based on the KOSI (Kometensimulation) experiments (Huebner, 2006). In this work we have chosen two values,  $2 \times 10^{-4}$  and  $10^{-1}$ , which lead to a thermal inertia of about 15 TIU and of about 500 TIU, respectively. The thermal inertia of 15 TIU probably is the best-known value of this parameter (Rivkin et al., 2011), and it is used in many previous thermal modeling, that is, Hayne and Aharonson (2015), Landis et al. (2017), and Schorghofer et al. (2017). The albedo of the ice-rich patch is calculated according to the volumetric percentage of rock (85%) and ice (15%). The bolometric albedo is calculated starting from the single scattering albedo (SSA) of the water ice and of the dark regolith, accordingly to Ciarniello et al. (2017) and Hapke (2012).

## 2.2. Shape Model and Mesh

We use the Ceres’ shape model derived on the basis of the images acquired by the Framing Camera (Preusker et al., 2016) during the Survey mission phase. We report in Figure 1a a portion of Ceres’ surface containing the Oxo crater and in Figure 1b the 3-D reconstruction of Oxo by using the software COMSOL Multiphysics.

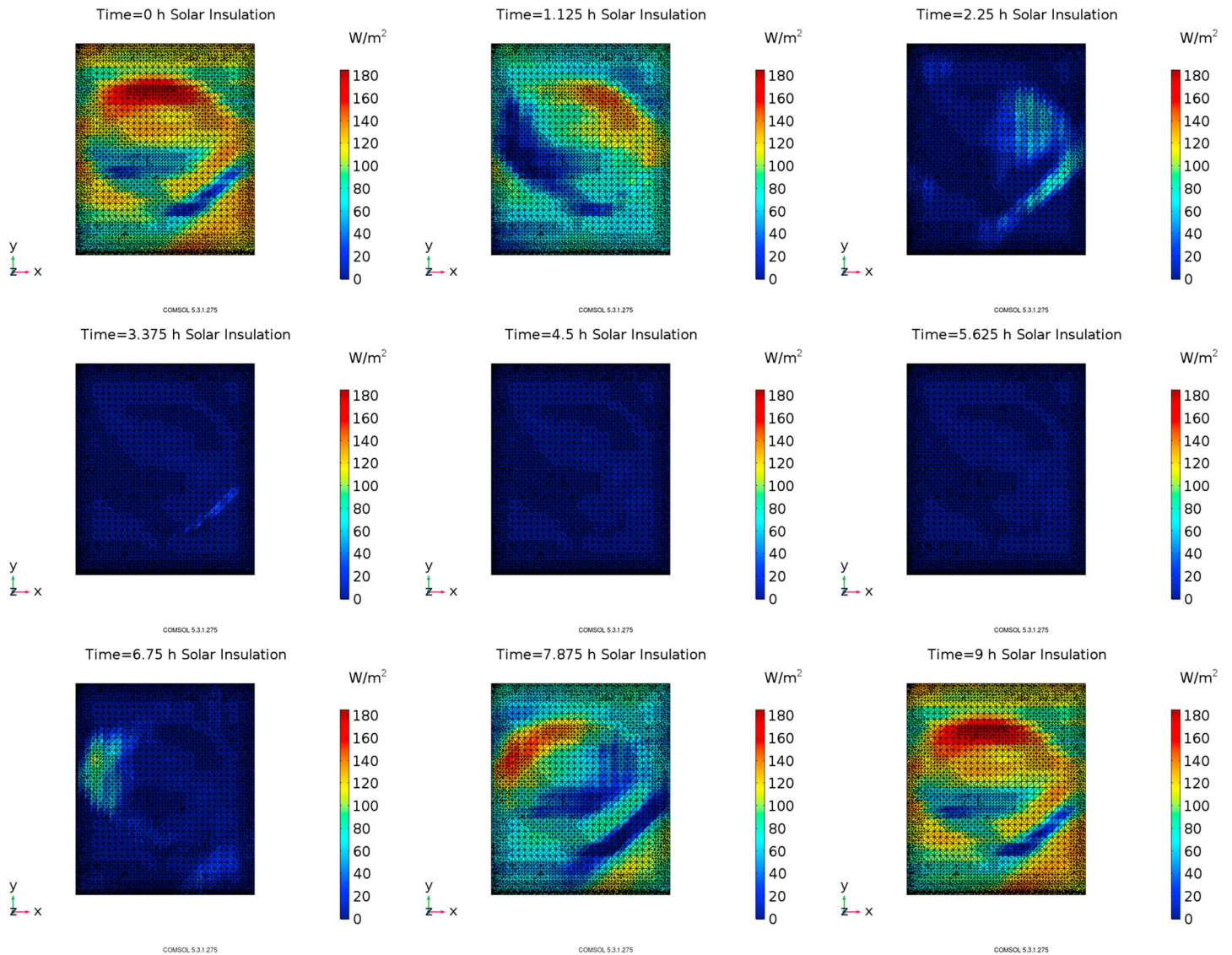


**Figure 2.** Incoming solar radiation in  $W\ m^{-2}$  at 2.71 AU during a Cerean day.

The digital terrain model (DTM) we used in these simulations is provided by the Ceres' shape model (Preusker et al., 2016): we processed the shape model data into a format and resolution suitable for the numerical code we have used. The original data have been processed and triangulated with an average size of 500 m and converted in a stereolithography file, which has been ingested into the COMSOL software suite. The stereolithography file is provided in the supporting information. Top (surface) and bottom sides of the 3-D reconstruction is meshed with free triangles (17,050), while free quadrilaterals are used on the lateral sides. The appropriate mesh element size is automatically set by the software COMSOL Multiphysics on the basis of the physical equations involved and on the Oxo geometry. The minimum element size is about 26 m, while the maximum is about 605 m. Beneath the top side, eight boundary layers are included, with a total thickness of 1 cm and a stretching factor of 1.2. The number of degrees of freedom is 84,569. The integration time step is about 2 min.

### 2.3. Illumination Conditions

Illumination on the shape model is calculated applying a rotational matrix to a 3-D object. In particular, for each facet we multiplied the components of the normal vector ( $n_x$ ,  $n_y$ , and  $n_z$ ) by the rotation matrix  $\vec{R}$ , whose

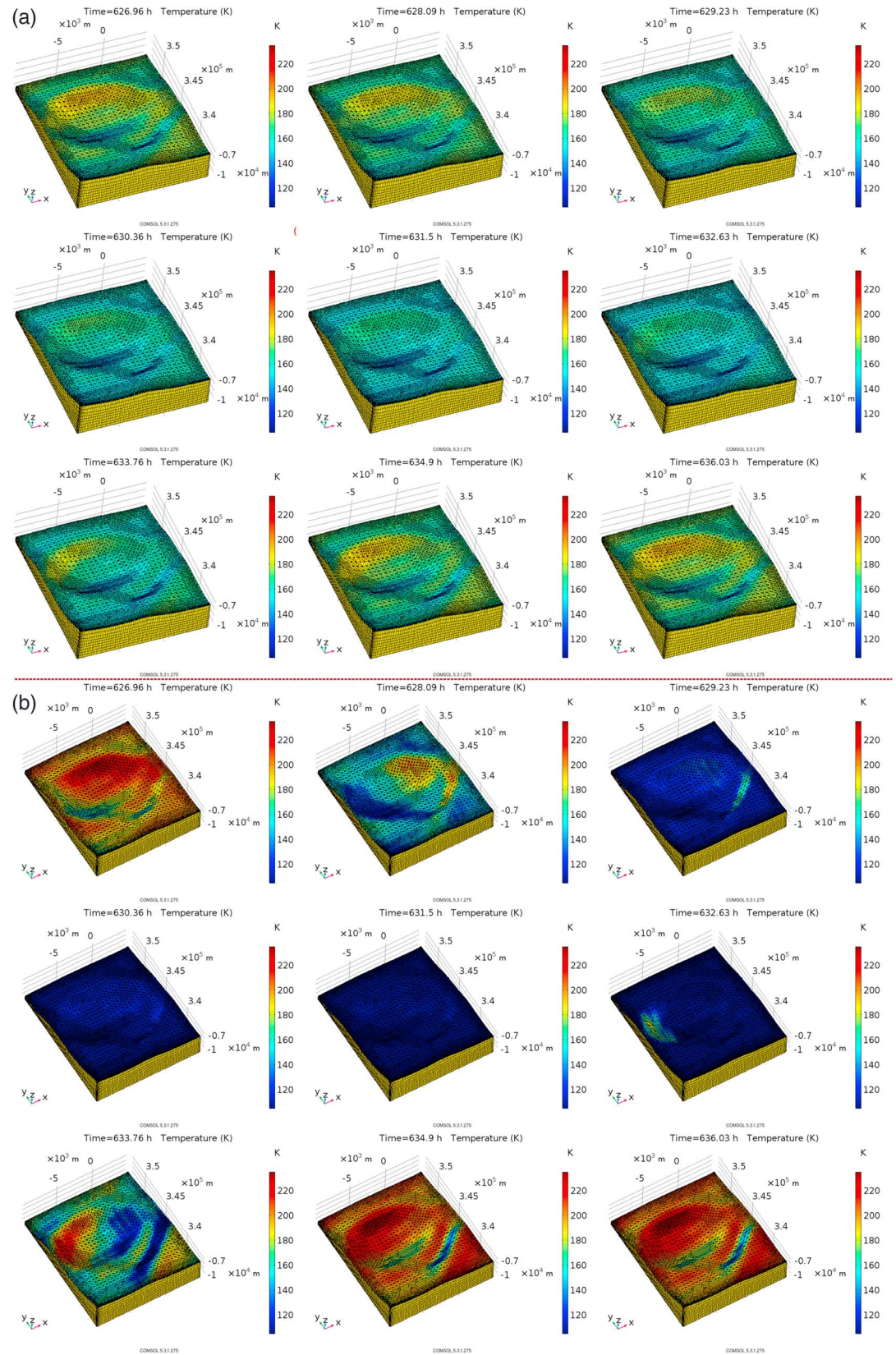


**Figure 3.** Surface temperatures at heliocentric distance (2.71 AU) of Herschel measurements (Küppers et al., 2014) in case of thermal inertia 500 TIU (top panels—*a*) and 15 TIU (bottom panels—*b*). Figures cover a full Cerean day: each figure is at 1 hr from the other. Color scale on the right refers to temperatures in Kelvin degrees.

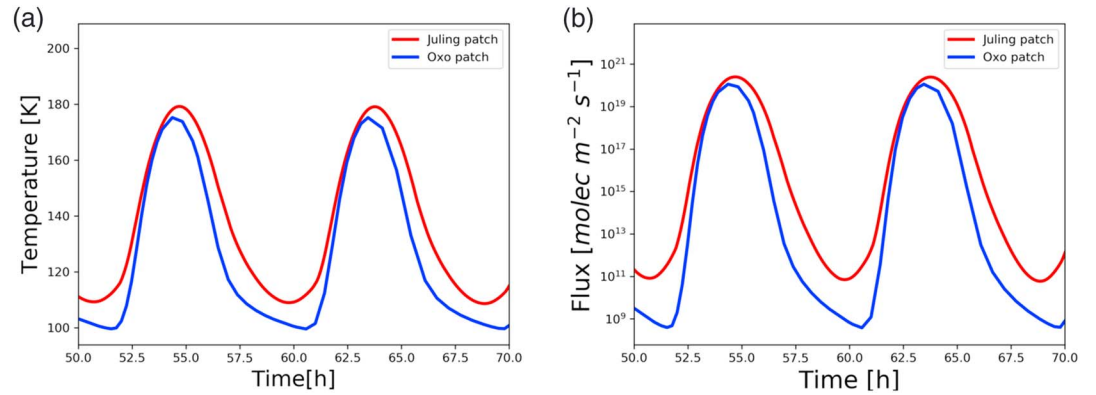


**Figure 4.** Comparison between the ice-rich patch temperatures (panel a) of Oxo (blue line) and Juling (red line) and water sublimation rate (panel b) are reported. The calculation is performed at 2.71 AU and with thermal inertia of 15 TIU.

components ( $k_x$ ,  $k_y$ , and  $k_z$ ) are given by

$$\begin{cases} k_x = -\cos(\Theta)\sin(\beta)\cos(\omega t) + \cos(\beta)\sin(\omega t) \\ k_y = \cos(\Theta)\sin(\alpha) [\sin(\beta)\sin(\omega t) - \cos(\beta)\cos(\omega t)] \\ k_z = \cos(\Theta)\cos(\alpha) [\cos(\beta)\cos(\omega t) - \sin(\beta)\sin(\omega t)], \end{cases} \quad (8)$$

where  $\Theta$  is the subsolar point latitude,  $\alpha$  and  $\beta$  are the coordinates of Oxo, and  $\omega$  is the angular velocity. Shadowing effects are computed by the hemicube method.

In Figure 2 we report the solar irradiance in watts per square meter on Oxo's surface at 2.71 AU. Images of Figure 2 are at 1 hr each from the other. The southern ice-rich patch results in both cases weakly illuminated compared to the other regions of the crater during all the Cerean day.

### 3. Results

In this section we analyzed the surface temperatures and water vapor production rates for the three different scenarios, whose characteristics are reported in Table 1. In order to achieve a stationary state we perform several planetary rotations at a fixed heliocentric distance, the same method adopted in Formisano et al. (2018).

#### 3.1. Cases A1 and A2: 2.71 AU—Herschel Comparison

We start to discuss the results of the scenarios A1 and A2, in which the chosen distance is compatible with the distance at which Herschel carried out its 24 October 2012 measurements (Küppers et al., 2014), that is, 2.71 AU. The results are shown in Figure 3, in which the top panels refer to the case of thermal inertia 500 TIU (case A1), while the bottom panels to 15 TIU (case A2). Time step between the frames is  $\approx 1$  hr and a fully Cerean day ( $\approx 9$  hr) is covered.

A noticeable difference between these two cases (A1 and A2) is the minimum and maximum values of temperature reached during the Cerean day and it is due to the different thermal inertia values that affect the way in which the surface reacts to the solar input (see Hayne & Aharonson, 2015). In case of low thermal inertia (15 TIU—A2), the maximum and minimum values in the floor are 104 and 215 K, respectively, with an average value of 147 K. Conversely, in case of high thermal inertia (500 TIU—A1), the “day-night” temperature profile

**Table 3**

*Ice-Rich Patches on Oxo and Juling: Temperatures (Min, Max and Mean), Mean Water Vapor Rate Production (in Molecules for per Square Meter and per Second and for Planetary Rotation, i.e., 9 hr), Mean Lifetime ( $\tau$ ) of Ice at 1 cm Beneath the Surface*

| Crater | Latitude | $T_{\min}$ (K) | $T_{\max}$ (K) | $\langle T \rangle$ (K) | Mean rate (molecules per square meter per second) | Rate (mm/[9 hr])     | $\tau$ (Earth years)      |
|--------|----------|----------------|----------------|-------------------------|---|----------------------|---------------------------|
| Juling | 35 S     | 109            | 179            | 143                     | $7.4 \times 10^{17}$                              | $7.8 \times 10^{-4}$ | $\approx 13$              |
| Oxo    | 42 N     | 99             | 175            | 129                     | $7.7 \times 10^{15}$                              | $8 \times 10^{-6}$   | $\approx 1.3 \times 10^3$ |

*Note.* Mean values are calculated over the whole period by using the equation (3). Comparison is carried out at 2.71 AU and thermal inertia, at 15 TIU.

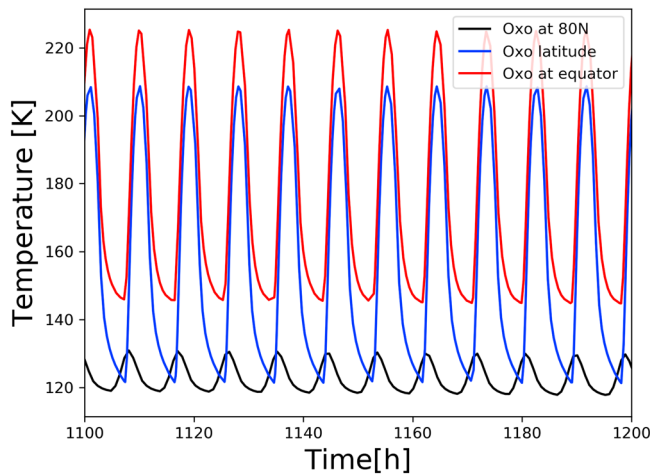


**Figure 5.** Surface temperatures of Oxo (blue line) and “two hypothetical Oxo” virtually located at equator (black line) and at 80° N (red line). The calculation is performed at 2.71 AU and thermal inertia is equal to 15 TIU.

15 TIU. We used the DTM and the physical parameters for Juling already applied in Formisano et al. (2018). Ice-rich patch reaches in case of Juling a maximum value of about 179 K, while in case of Oxo a maximum of about 175 K. The diurnal variation of Juling temperature in the ice-rich patch region is about 10 K less than that in Oxo (see Figure 4a). If we calculate the sublimation rate in molecules per square meter and per second (see Figure 4b), we obtain a mean value for Juling about 2 orders of magnitude greater than for Oxo. With these production rates the lifetime of water ice within 1 cm from the surface is only few orbits (13 Earth years) in case of Juling and about 1,300 Earth years in case of Oxo. The maximum sublimation rates are very similar both for Oxo and Juling:  $1 \times 10^{20}$  and  $2.5 \times 10^{20}$ . Results are summarized in Table 3.

### 3.1.2. The Effects of the Latitude

In order to see the effects of the latitude on the calculation of surface temperatures and water vapor production, we virtually located Oxo at the equator and at latitude 80° N. In Figure 5 we report the average temperature of the floor: calculations are made at 2.71 AU and with thermal inertia 15 TIU. As already noted by Landis et al. (2017), the effects of local topography are very important in the estimation of water vapor

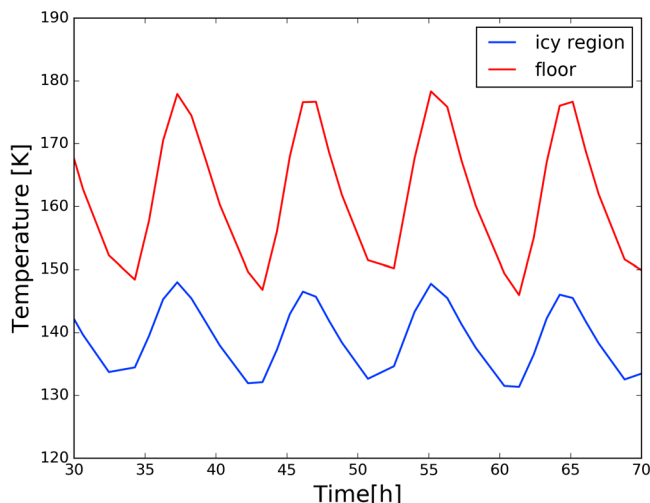


**Figure 6.** Average temperature of the ice-rich southern patch and of the floor. Calculations are performed at 2.96 AU and for thermal inertia 15 TIU.

tends to be more flat, with minimum and maximum values of 156 and 178 K, respectively. The average temperature of the floor, in this case, is 166 K. The values in case of low thermal inertia are compatible with the mean temperature obtained in the paper of Hayne and Aharonson (2015).

In both cases the ice-rich area in the southern wall is weakly illuminated by the Sun. The average temperature is 148 K in case A1 and 129 K in case A2. If we calculate the mean value over the whole period, we obtain a value of  $2 \times 10^{-4}$  mm per Cerean day in case A1 and  $8 \times 10^{-6}$  mm per Cerean day in case A2. This means that to erode a “icy-line” of 1 cm (compatible with the diurnal skin depth) it takes  $\approx 5 \times 10^4$  Earth years in case A1 and  $\approx 1.3 \times 10^3$  Earth years in case A2. The sublimation rate in molecules per square meter per second is  $2 \times 10^{14}$  for A1 and  $7.7 \times 10^{15}$  for A2. Maximum rates can be calculated by using the equation (3) by inserting the maximum temperature: we obtain  $8.8 \times 10^{17}$  molecules per square meter per second for A1 and  $1 \times 10^{20}$  molecules per square meter per second for A2. The range of variability of the temperature in the ice-rich region is 144–154 K in A1 and 99–175 K in A2.

### 3.1.1. Comparison With the Juling Ice-Rich Patch

It is interesting to compare the results obtained for the ice-rich patches of Oxo and Juling. The comparison is made at 2.71 AU and thermal inertia

of the local topography at the same latitude. From Figure 5 we observe that a crater with the same topography of Oxo at equator would be characterized by a maximum temperature of about 220 K, 20 K greater than the average surface temperature of the “real” Oxo. The same crater at 80° N very near to the pole, experiences a very weak sun illumination: its day-night profile is very flat and its average surface temperature is close to 130 K. We can deduce that a difference of about 90 K exists between the maximum temperature of a crater at equator and at 80° poleward, while in Hayne and Aharonson (2015) is obtained a difference of 100 K without taking into account the real local topography.

### 3.2. Case A3: 2.96 AU—VIR Comparison

The last case explored is the one at heliocentric distance 2.96 AU, since it is the distance at which we have VIR data to retrieve the surface temperatures. Numerical results give a temperature profile shown in Figure 6. Thermal inertia in this case is 15 TIU. The average temperature of the ice-rich patch on the southern wall is  $\approx 142$  K, while the floor has an average

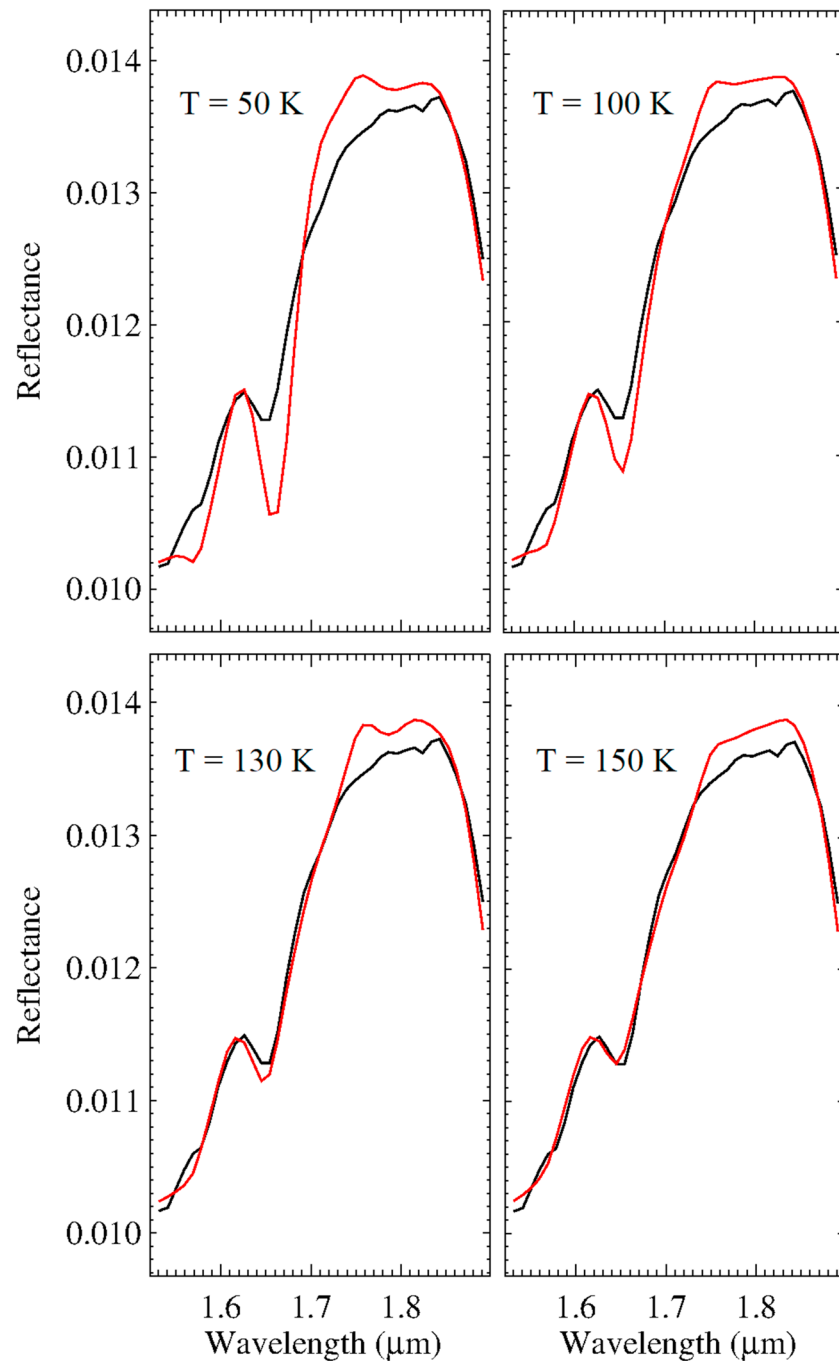


**Figure 7.** Different best fits (red lines) of the measured icy spectrum (black line) are performed by means of optical constants measured at different temperatures Mastrapa et al. (2008, 2009) with a sampling step of 10 K from 50 to 150 K. The best fit is obtained for optical constants measured at  $T = 150\text{ K}$ .

temperature of 163 K. To make a comparison, in the following we will discuss VIR measurements of the average temperatures of the floor and of the icy patch.

### 3.2.1. Water Ice Temperature Retrieval

Temperature analysis is performed by taking into account the spectral variation of crystalline water ice as a function of the temperature. In particular we focused on the spectral region 1.5–1.9  $\mu\text{m}$ , which is more sensitive to temperature changes according to Mastrapa et al. (2008, 2009). Water ice has been detected with the VIR spectrometer on board Dawn during the Low Altitude Mapping Orbit phase of the mission, at 2.96 AU, and at 9.5-hr local solar time. We performed the spectral modeling of an average spectrum of the water-rich

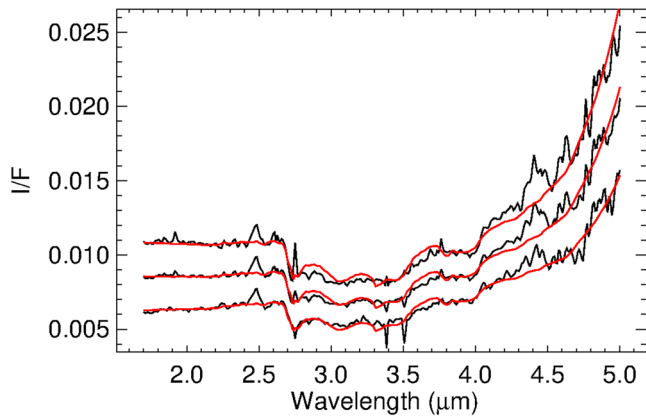


**Figure 8.** Average spectrum of the Oxo crater floor  $\pm$  standard deviation of the signal (black lines). The models (red lines) are obtained with temperature of 165, 169.5, and 172.5 K (from the bottom).

region using the Hapke radiative transfer model (Hapke, 2012) in order to retrieve the water ice properties. Method and results of the modeling are reported in Raponi, De Sanctis, Frigeri, et al. (2018). Taking as input different optical constants, measured at different temperature, we obtained different fits to the measured spectrum. The best fit is obtained with optical constants measured at  $150 \pm 5$  K, as we can see in Figure 7. The uncertainty is due to the sampling of 10 K of the measured optical constants (Mastrapa et al., 2008, 2009).

### 3.2.2. Crater Floor Temperature Retrieval

We take into account an average spectrum of the crater floor detected by the Dawn's VIR during the Low Altitude Mapping Orbit phase at 2.96 AU and at 9.5-hr local solar time. The total radiance is modeled by accounting for both the contributions of the reflected sunlight and the thermal emission:

$$\text{Rad} = r \frac{F_{\text{sol}}}{D^2} + \epsilon_d B(\lambda, T), \quad (9)$$

where  $r$  is the Hapke bidirectional reflectance (see Raponi, De Sanctis, Frigeri, et al., 2018, for the details on the modeling),  $F_{\text{sol}}$  is the solar irradiance at 1 AU,  $D$  is the heliocentric distance (AU),  $\epsilon_d$  is the directional emissivity (Hapke, 2012), and  $B(\lambda, T)$  is the Planck function. With an optimization algorithm we obtained a best fit with a temperature of 169.5 K. The best fit is also performed for the spectra obtained by subtracting/adding the standard deviation of the signal to the average spectrum. In this way we obtained a lower/upper limit of 165/172.5 K. Results are shown in Figure 8. We note that for both ice-rich patch and crater floor VIR measurements return a mean temperature, which is in agreement with our numerical simulations, supporting the fact that low thermal inertia (i.e., 15 TIU) can characterize Ceres' surface.

## 4. Conclusions

In this paper we have studied the illumination conditions, and consequently the surface temperatures, of a particular location of the northern hemisphere ( $42^\circ$ ) of Ceres' surface, that is, the Oxo crater (Combe et al., 2016, 2018; Raponi et al., 2016). We have used the real topography of the crater as well as we have included self-heating effects in the energy balance. As revealed by the Dawn's VIR measurements, the southern wall of this crater exhibits spectral evidence of water ice, similarly to another crater of the southern hemisphere, the Juling crater (Combe et al., 2016; Raponi, De Sanctis, Carrozzo, et al., 2018). Our numerical simulations show as "low" values of thermal inertia (15 TIU) are necessary to recover a large day-night amplitude, while very high values (500 TIU) lead to a relatively flat profile, in agreement with the results obtained by Hayne and Aharonson (2015). In case of thermal inertia 15 TIU, at the distance compatible with the Herschel measurements (2.71 AU), the surface temperature ranges from 104 to 215 K in the floor, while the southern ice-rich wall has an average temperature of 129 K. If we calculate the mean sublimation rate over the whole rotation we obtain a value of  $7.7 \times 10^{15}$  molecules per square meter per second. Considering that the ice coverage is  $< 10 \text{ km}^2$  (Combe et al., 2018), we obtain an emission rate significantly  $< 1 \text{ kg s}^{-1}$ , well below the Herschel emission ( $6 \text{ kg s}^{-1}$ ). This means that a large emitting area is required and the only southern wall is not sufficient to supply a water ice emission rate compatible with the Herschel measures (Küppers et al., 2014). Assuming that the whole crater (area of  $8 \times 10^7 \text{ m}^2$ ) emits, we do not recover the Herschel water vapor rate, obtaining a value of the order of  $10^{23}$  molecules per second. We can note that a comparison with the Juling crater, at the same thermophysical conditions, lead to an emission rate of  $7.4 \times 10^{17}$  molecules per square meter per second, 2 orders of magnitude greater for Juling. Maximum rates, instead, are very similar and of the order of  $10^{20}$  molecules per square meter per second. Considering that Juling is 20 km in diameter (area of  $3 \times 10^8 \text{ m}^2$ ) and assuming that the whole crater contributes to the water vapor emission, we obtain a value very close to the Herschel detection (Küppers et al., 2014).

Our numerical results performed at 2.96 AU, with thermal inertia 15 TIU, indicates an average temperature of 142 and 163 K for the ice-rich patch and for the floor, respectively. These values are in agreement, in the limit of the error, with the VIR measurements, which return a value of  $150 \pm 5$  K for the patch and a lower/upper limit of 165/172.5 K for the floor. It is also interesting to see the effects of the latitude on the surface temperature.

An hypothetical Oxo at the equator experiences temperatures as high as 220 K (in the floor). Conversely, near the pole, the day-night profile becomes relatively flat, with an average temperature of the floor of 140 K.

Our numerical simulations suggest that the mean emission rate of the Oxo ice-rich patch is not sufficient to justify the Herschel measurements ( $10^{26}$  molecules per second or equivalently  $6 \text{ kg s}^{-1}$ ; Küppers et al., 2014), even if we consider that also the crater floor contributed to the water emission, due to the smaller size of Oxo respect Juling. Probably, the Juling crater is more likely than Oxo to represent the source of the water vapor emission detected by Herschel.

#### Acknowledgments

This work is supported by an ASI (Agenzia Spaziale Italiana) grant. We would like to thank two anonymous referees for the useful comments and suggestions. Data table and DTM are listed in the repository: <https://github.com/MiFormisano/miformisano>.

#### References

- A'Hearn, M. F., & Feldman, P. D. (1992). Water vaporization on Ceres. *Icarus*, 98, 54–60. [https://doi.org/10.1016/0019-1035\(92\)90206-M](https://doi.org/10.1016/0019-1035(92)90206-M)
- Bland, M. T., Raymond, C. A., Schenk, P. M., Fu, R. R., Kneissl, T., Pasckert, J. H., et al. (2016). Composition and structure of the shallow subsurface of Ceres revealed by crater morphology. *Nature Geoscience*, 9, 538–542. <https://doi.org/10.1038/ngeo2743>
- Carrozzo, F. G., De Sanctis, M. C., Raponi, A., Ammannito, E., Castillo-Rogez, J., Ehlmann, B. L., et al. (2018). Nature, formation, and distribution of carbonates on Ceres. *Science Advances*, 4(3), e1701645. <https://doi.org/10.1126/sciadv.1701645>
- Castillo-Rogez, J. C., & McCord, T. B. (2010). Ceres' evolution and present state constrained by shape data. *Icarus*, 205, 443–459. <https://doi.org/10.1016/j.icarus.2009.04.008>
- Ciarniello, M., De Sanctis, M. C., Ammannito, E., Raponi, A., Longobardo, A., Palomba, E., et al. (2017). Spectrophotometric properties of dwarf planet Ceres from the VIR spectrometer on board the Dawn mission. *Astronomy & Astrophysics*, 598, A130. <https://doi.org/10.1051/0004-6361/201629490>
- Combe, J.-P., McCord, T. B., Tosi, F., Ammannito, E., Carrozzo, F. G., De Sanctis, M. C., et al. (2016). Detection of local H<sub>2</sub>O exposed at the surface of Ceres. *Science*, 353, aaf3010. <https://doi.org/10.1126/science.aaf3010>
- Combe, J.-P., Raponi, A., Tosi, F., De Sanctis, M.-C., Carrozzo, F.-G., Zambon, F., et al. (2018). Exposed H<sub>2</sub>O-rich areas detected on Ceres with the Dawn Visible and InfraRed mapping spectrometer. *Icarus*, 318, 22–41. <https://doi.org/10.1016/j.icarus.2017.12.008>
- De Sanctis, M. C., Raponi, A., Ammannito, E., Ciarniello, M., Toplis, M. J., McSween, H. Y., et al. (2016). Bright carbonate deposits as evidence of aqueous alteration on (1) Ceres. *Nature*, 536, 54–57. <https://doi.org/10.1038/nature18290>
- Delsemme, A. H., & Miller, D. C. (1971). The continuum of Comet Burnham (1960 II): The differentiation of a short period comet. *Planetary and Space Science*, 19, 1229–1257. [https://doi.org/10.1016/0032-0633\(71\)90180-2](https://doi.org/10.1016/0032-0633(71)90180-2)
- Ellsworth, K., & Schubert, G. (1983). Saturn's icy satellites—Thermal and structural models. *Icarus*, 54, 490–510. [https://doi.org/10.1016/0019-1035\(83\)90242-7](https://doi.org/10.1016/0019-1035(83)90242-7)
- Ermakov, A. I., Fu, R. R., Castillo-Rogez, J. C., Raymond, C. A., Park, R. S., Preusker, F., et al. (2017). Constraints on Ceres' internal structure and evolution from its shape and gravity measured by the Dawn spacecraft. *Journal of Geophysical Research: Planets*, 122, 2267–2293. <https://doi.org/10.1002/2017JE005302>
- Fanale, F. P., & Salvail, J. R. (1987). The loss and depth of CO<sub>2</sub> ice in comet nuclei. *Icarus*, 72, 535–554. [https://doi.org/10.1016/0019-1035\(87\)90051-0](https://doi.org/10.1016/0019-1035(87)90051-0)
- Formisano, M., De Sanctis, M. C., Magni, G., Federico, C., & Capria, M. T. (2016). Ceres water regime: Surface temperature, water sublimation and transient exo(atmo)sphere. *Monthly Notices of the Royal Astronomical Society*, 455, 1892–1904. <https://doi.org/10.1093/mnras/stv2344>
- Formisano, M., Federico, C., De Angelis, S., De Sanctis, M. C., & Magni, G. (2016). The stability of the crust of the dwarf planet Ceres. *Monthly Notices of the Royal Astronomical Society*, 463, 520–528. <https://doi.org/10.1093/mnras/stw1910>
- Formisano, M., Federico, C., De Sanctis, M. C., Frigeri, A., Magni, G., Raponi, A., & Tosi, F. (2018). Thermal stability of water ice in Ceres' craters: The case of Juling crater. *Journal of Geophysical Research: Planets*, 123, 2445–2463. <https://doi.org/10.1029/2017JE005417>
- Fu, R. R., Ermakov, A. I., Marchi, S., Castillo-Rogez, J. C., Raymond, C. A., Hager, B. H., et al. (2017). The interior structure of Ceres as revealed by surface topography. *Earth and Planetary Science Letters*, 476, 153–164. <https://doi.org/10.1016/j.epsl.2017.07.053>
- Hapke, B. (2012). *Theory of reflectance and emittance spectroscopy* (2nd ed.). Cambridge: Cambridge University Press. <https://doi.org/10.1017/CBO9781139025683>
- Hayne, P. O., & Aharonson, O. (2015). Thermal stability of ice on Ceres with rough topography. *Journal of Geophysical Research: Planets*, 120, 1567–1584. <https://doi.org/10.1002/2015JE004887>
- Heiken, G. H., Vaniman, D. T., & French, B. M. (1991). *Lunar sourcebook—A user's guide to the Moon*. Cambridge University Press.
- Huebner, W. F. (2006). Heat and gas diffusion in comet nuclei (ISSI scientific report). International Space Science Institute.
- Keller, H. U., Mottola, S., Davidsson, B., Schröder, S. E., Skorov, Y., Kühr, E., et al. (2015). Insolation, erosion, and morphology of comet 67P/Churyumov-Gerasimenko. *Astronomy & Astrophysics*, 583, A34. <https://doi.org/10.1051/0004-6361/201525964>
- King, S. D., Castillo-Rogez, J. C., Toplis, M. J., Bland, M. T., Raymond, C. A., & Russell, C. T. (2018). Ceres internal structure from geophysical constraints. *Meteoritics & Planetary Science*, 53, 1999–2007. <https://doi.org/10.1111/maps.13063>
- Klinger, J. (1980). Influence of a phase transition of ice on the heat and mass balance of comets. *Science*, 209, 271. <https://doi.org/10.1126/science.209.4453.271>
- Komle, N. I., Macher, W., Tiefenbacher, P., Kargl, G., Pelivan, I., Knollenberg, J., et al. (2017). Three-dimensional illumination and thermal model of the Abydos region on comet 67P/Churyumov-Gerasimenko. *Monthly Notices of the Royal Astronomical Society*, 469(Suppl\_2), S2–S19. <https://doi.org/10.1093/mnras/stx561>
- Konopliv, A. S., Park, R. S., Vaughan, A. T., Bills, B. G., Asmar, S. W., Ermakov, A. I., et al. (2018). The Ceres gravity field, spin pole, rotation period and orbit from the Dawn radiometric tracking and optical data. *Icarus*, 299, 411–429. <https://doi.org/10.1016/j.icarus.2017.08.005>
- Küppers, M., O'Rourke, L., Bockelée-Morvan, D., Zakharov, V., Lee, S., von Allmen, P., et al. (2014). Localized sources of water vapour on the dwarf planet (1) Ceres. *Nature*, 505, 525–527. <https://doi.org/10.1038/nature12918>
- Landis, M. E., Byrne, S., Schörghofer, N., Schmidt, B. E., Hayne, P. O., Castillo-Rogez, J., et al. (2017). Conditions for sublimating water ice to supply Ceres' exosphere. *Journal of Geophysical Research: Planets*, 122, 1984–1995. <https://doi.org/10.1002/2017JE005335>
- Li, J.-Y., Reddy, V., Nathues, A., Le Corre, L., Izawa, M. R. M., Cloutis, E. A., et al. (2016). Surface albedo and spectral variability of Ceres. *Astrophysical Journal Letters*, 817, L22. <https://doi.org/10.3847/2041-8205/817/2/L22>
- Mastrapa, R. M., Bernstein, M. P., Sandford, S. A., Roush, T. L., Cruikshank, D. P., & Dalle Ore, C. M. (2008). Optical constants of amorphous and crystalline H<sub>2</sub>O-ice in the near infrared from 1.1 to 2.6  $\mu\text{m}$ . *Icarus*, 197, 307–320. <https://doi.org/10.1016/j.icarus.2008.04.008>

- Mastrapa, R. M., Sandford, S. A., Roush, T. L., Cruikshank, D. P., & Dalle Ore, C. M. (2009). Optical constants of amorphous and crystalline H<sub>2</sub>O-ice: 2.5–22 μm (4000–455 cm<sup>-1</sup>) optical constants of H<sub>2</sub>O-ice. *Astrophysical Journal*, *701*, 1347–1356. <https://doi.org/10.1088/0004-637X/701/2/1347>
- McCord, T. B., & Sotin, C. (2005). Ceres: Evolution and current state. *Journal of Geophysical Research*, *110*, E05009. <https://doi.org/10.1029/2004JE002244>
- McSween, H. Y., Emery, J. P., Rivkin, A. S., Toplis, M. J., Castillo-Rogez, J. C., Prettyman, T. H., et al. (2018). Carbonaceous chondrites as analogs for the composition and alteration of Ceres. *Meteoritics & Planetary Science*, *53*, 1793–1804. <https://doi.org/10.1111/maps.12947>
- Murphy, D. M., & Koop, T. (2005). Review of the vapour pressures of ice and supercooled water for atmospheric applications. *Quarterly Journal of the Royal Meteorological Society*, *131*(608), 1539–1565. <https://doi.org/10.1256/qj.04.94>
- Nathues, A., Hoffmann, M., Platz, T., Thangjam, G. S., Cloutis, E. A., Reddy, V., et al. (2016). FC colour images of dwarf planet Ceres reveal a complicated geological history. *Planetary and Space Science*, *134*, 122–127. <https://doi.org/10.1016/j.pss.2016.10.017>
- Nathues, A., Platz, T., Hoffmann, M., Thangjam, G., Cloutis, E. A., Applin, D. M., et al. (2017). Oxo crater on (1) Ceres: Geological history and the role of water-ice. *Astronomical Journal*, *154*(84), 13. <https://doi.org/10.3847/1538-3881/aa7a04>
- Neveu, M., & Desch, S. J. (2015). Geochemistry, thermal evolution, and cryovolcanism on Ceres with a muddy ice mantle. *Geophysical Research Letters*, *42*, 10,197–10,206. <https://doi.org/10.1002/2015GL066375>
- Park, R. S., Konopliv, A. S., Bills, B., Castillo-Rogez, J., Asmar, S. W., Rambaux, N., et al. (2016). A partially differentiated interior for (1) Ceres deduced from its gravity field and shape. *Nature*, *537*, 515–517. <https://doi.org/10.1038/nature18955>
- Platz, T., Nathues, A., Schorghofer, N., Preusker, F., Mazarico, E., Schröder, S. E., et al. (2016). Surface water-ice deposits in the northern shadowed regions of Ceres. *Nature Astronomy*, *1*, 7. <https://doi.org/10.1038/s41550-016-0007>
- Prettyman, T. H., Yamashita, N., Toplis, M. J., McSween, H. Y., Schörghofer, N., Marchi, S., et al. (2017). Extensive water ice within Ceres' aqueously altered regolith: Evidence from nuclear spectroscopy. *Science*, *355*(6320), 55–59. <https://doi.org/10.1126/science.aah6765>
- Preusker, F., Scholten, F., Matz, K.-D., Elgner, S., Jaumann, R., Roatsch, T., et al. (2016). Dawn at Ceres: Shape model and rotational state. In *Lunar and planetary science conference* (Vol. 47, pp. 1954). The Woodlands, TX. Retrieved from <https://adsabs.harvard.edu/abs/2016LPI...47.1954P>
- Raponi, A., Carrozzo, F. G., Zambon, F., De Sanctis, M. C., Ciarniello, M., Frigeri, A., et al. (2017). Mineralogical mapping of Coniraya quadrangle of the dwarf planet Ceres. *Icarus*, *318*, 99–110. <https://doi.org/10.1016/j.icarus.2017.10.023>
- Raponi, A., De Sanctis, M. C., Carrozzo, F. G., Ciarniello, M., Castillo-Rogez, J. C., Ammannito, E., et al. (2018). Mineralogy of Occator crater on Ceres and insight into its evolution from the properties of carbonates, phyllosilicates, and chlorides. *Icarus*. <https://doi.org/10.1016/j.icarus.2018.02.001>
- Raponi, A., De Sanctis, M. C., Ciarniello, M., Ammannito, E., Frigeri, A., Combe, J.-P., et al. (2017). Water ice on Ceres' surface as seen by Dawn-VIR: Properties retrieval by means of spectral modeling. In *Lunar and planetary science conference, Lunar and Planetary Inst. Technical Report*, 48 (pp. 2007). The Woodlands, TX.
- Raponi, A., De Sanctis, M. C., Ciarniello, M., Tosi, F., Combe, J.-P., Frigeri, A., et al. Dawn/VIR Team (2016). Spectral modeling of water ice-rich areas on Ceres' surface from Dawn-VIR data analysis: Abundance and grain size retrieval. In *Aas/division for planetary sciences meeting Abstracts #48* (pp. 506.07). Pasadena, CA.
- Raponi, A., De Sanctis, M. C., Frigeri, A., Ammannito, E., Ciarniello, M., Formisano, M., et al. (2018). Variations in the amount of water ice on Ceres' surface suggest a seasonal water cycle. *Science Advances*, *4*(3), eaao3757. <https://doi.org/10.1126/sciadv.aao3757>
- Rivkin, A. S., Li, J.-Y., Milliken, R. E., Lim, L. F., Lovell, A. J., Schmidt, B. E., et al. (2011). The surface composition of Ceres. *Space and Science Review*, *163*, 95–116. <https://doi.org/10.1007/s11214-010-9677-4>
- Russell, C. T., Raymond, C. A., Konopliv, A. S., Park, R. S., Polansky, C., Rayman, M. D., & Castillo-Rogez, J. C. (2016). Dawn arrives at Ceres: Exploration of a small, volatile-rich world. *Science*, *353*, 1008–1010. <https://doi.org/10.1126/science.aaf4219>
- Schmidt, B. E., Hughson, K. H. G., Chilton, H. T., Scully, J. E. C., Platz, T., Nathues, A., et al. (2017). Geomorphological evidence for ground ice on dwarf planet Ceres. *Nature Geoscience*, *10*, 338–343. <https://doi.org/10.1038/ngeo2936>
- Schorghofer, N., Byrne, S., Landis, M. E., Mazarico, E., Prettyman, T. H., Schmidt, B. E., et al. (2017). The putative Cerean exosphere. *Astrophysical Journal*, *850*, 85. <https://doi.org/10.3847/1538-4357/aa932f>
- Schorghofer, N., Mazarico, E., Platz, T., Preusker, F., Schröder, S. E., Raymond, C. A., & Russell, C. T. (2016). The permanently shadowed regions of dwarf planet Ceres. *Geophysical Research Letters*, *43*, 6783–6789. <https://doi.org/10.1002/2016GL069368>
- Shi, X., Hu, X., Sierks, H., Güttler, C., A'Hearn, M., Blum, J., et al. (2016). Sunset jets observed on comet 67P/Churyumov-Gerasimenko sustained by subsurface thermal lag. *Astronomy & Astrophysics*, *586*, A7. <https://doi.org/10.1051/0004-6361/201527123>
- Titus, T. N. (2015). Ceres: Predictions for near-surface water ice stability and implications for plume generating processes. *Journal of Geophysical Research: Planets*, *42*, 2130–2136. <https://doi.org/10.1002/2015GL063240>
- Villarreal, M. N., Russell, C. T., Luhmann, J. G., Thompson, W. T., Prettyman, T. H., A'Hearn, M. F., et al. (2017). The dependence of the cerean exosphere on solar energetic particle events. *The Astrophysical Journal Letters*, *838*(1), L8.